DOI: 10.36108/ujees/2202.40.0180
UNIOSUN Journal of Engineering and Environmental Sciences. Vol. 4 No. 1. March. 2022

Fluid Velocity Profile in Ascending and Descending Layer Heterogeneous Porous Media

Alabi, O.O. and Akanni, I.A.

Abstract: A laboratory experiment with the heterogeneous layered medium has been extended to the concept of flow units in hydrocarbon reservoir systems based on the established refraction-like property of fluids at the interface of two media of different porosities. The purpose of this research is to improve the accuracy of reservoir systems models by this extension. Numerical simulation was applied on both Ascending Layer Heterogenous (ALH) and Descending Layer Heterogenous (DLH) experimental data, to obtain the properties of each layered system and deduce models. This research shows that when fluid flows from a unit of lower to higher porosity unit, referred to as ALH, a maximum volume flux is experienced at higher deflection angles from normal. This tendency increases with the increase in porosity difference. On the other hand, a flow from a flow unit of higher to that of a lower porosity, referred to as DLH will result in the maximum volume flux being experienced at the normal with decreasing magnitude as the deviation increases from normal. In addition, the flow becomes more chaotic and less predictable with an increase in porosity difference in both ALH and DLH. Furthermore, two methods of models combination to obtain a single generalized model were explored. For ALH, the Vector Space Model (VSM) and New Model (NM) could be used interchangeably because of the negligible difference in their mean absolute error. At the same time, for the DLH, only the VSM is more appropriate.

Keywords: Deflection angle, New model, Porosity, Porous media, Vector space model

I. Introduction

Fluid flow through a homogenous porous medium can be explained with Darcy law. This relates the volume flux with the volumetric flow rate, and the boundary area holding the medium; for laminar flow [1], [2]. This relationship is expressed as:

$$q = \frac{Q}{A} = K.i \quad (1)$$

where q is the volume flux (m/s), sometimes wrongly assumed as seepage velocity. But the actual average pore water velocity is obtained from equation (2). This shows how much porosity influences fluid transport in porous media [3], [4]:

Alabi, O.O. and Akanni, I.A. (Solid Earth Physics Research Laboratory, Department of Physics, Osun State University, Osogbo, Osun State, Nigeria)
Corresponding author: : olusegun.alabi@uniosun.edu.ng
Phone Number: :+2348033541739
Submitted:11-01-2022
Accepted:22-02-2022

$$V = \frac{Q}{A\phi} = \frac{q}{\phi} \quad (2)$$

Q is the volumetric flow rate (m^3s^{-1}), A is the average cross-sectional area perpendicular to the line of flow (m^2), v is the seepage velocity (ms^{-1}), and ϕ is the porosity of the medium.

Permeability (k) can then be obtained from hydraulic conductivity (K) using the Hubert-King relation [4]:

$$k = \frac{\rho g}{A\mu} K \quad (3)$$

Where, ρ and μ are the fluid's density and viscosity respectively, and the other symbols denote the earlier mentioned parameters.

However, the relevance of the Darcian flow becomes inadequate to explain the heterogeneity property of soil or rocks; this heterogeneity property results from arbitrary changes in porosity in different directions and layers [1], [5]. Various studies have established and attempted to account for factors that

cause these changes, even in soils that are reasonably homogenous to the human eyes, aside from the known inverse relationship that exists between porosity and grain size, especially for irregularly shaped grains [6-7].

From the study of flow in remoulded loess specimens, it was observed that the arbitrary changes in porosity observed in nature have some contributions from bound water. This is more observable in instances where the pores' diameter is smaller than the thickness of the bound water around the particles that makes up the pore system of media [1]. This results in closely packed media particles, that prevent fluids from easily passing through. Also, the magnitude of the electrical field of the bound water determines the minimum velocity needed to break it free, and allow for free flow [8-9]. In addition, precipitation and minerals dissolution during fluid flow alter the pore system, resulting in a directly proportional increase in heterogeneous flow field as pore roughness increases [10-11]. This alteration process begins with nucleation and has a complex spatial distribution being influenced by factors like chemical properties, mass transport properties, mineralogy, temperature, pore morphology, and velocity of fluid flow [10–15].

It is of great importance to note that, the heterogeneity system in rocks is not static in most formations, leading to the classification of pores into primary (or dispositional) and secondary (or post-depositional) pores. It is this constant arbitrary changing secondary porosity system (vuggy, moldic, and fractures), due to generalized activities like solution flow, tectonic movement, and diagenesis, that cause complexity in rock structures [16-17]. Understanding the fluid flow properties at the interface of contact of different porosity regimes will therefore increase the accuracy of reservoir systems models.

In order to understand fluid transport properties at the interface of contact of different porosity regimes, like in-situ soil, and in oil reservoirs system now reported, it is important to beam light on the pore-scale system of fluid flow. Firstly, distinguishing between porosity and permeability is paramount. Porosity measures the amount of void in a medium, compared to the medium's bulk volume, while permeability measures ease of flow through such a medium [18–21]. Relative permeability can then be said to be directly proportional to porosity [22]–[24], but this is dependent on the morphological pore types being catenary and/or cul-de-sac pores [16]. However, [6] found this not to be always true, as physical factors affecting the correlation between these two parameters (permeability and porosity) also differ based on formation type. The onus is then on the petrol physicist and geologist to understand the specific formation being explored before assumptions are made. This is the purpose of downscaling into the pore-system of heterogeneous media [6], [25], [26]. It helps to shield more light on the fluid transport system, based on the porosity viz-a-viz permeability properties [2], [27], [28].

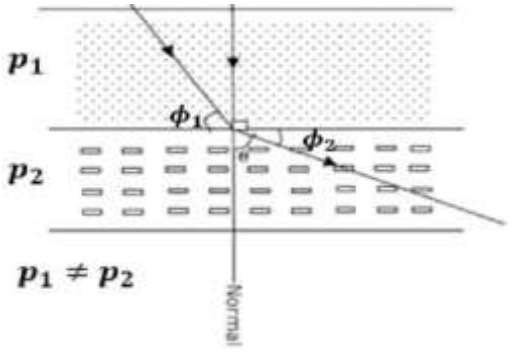

Figure 1: Schematic diagram to show the deflection angle (ϕ_2) adapted from [32]

Figure 1, illustrates the fluid transport system in a heterogeneous medium, at the pore scale, focusing on the flow pattern at the interface of contact between two different homogenous media. The first homogenous medium layer is

characterized by porosity p_1, while the bottom homogenous layer is characterized by porosity p_2. The deflection of the flow line follows the same pattern with the refraction of light, as stated earlier. It should be noted that $p_1 \neq p_2$.

The flow lines deflect to conform to the equation:

$$\frac{tan\phi_2}{tan\phi_1} = \frac{p_1}{p_2} \quad (4)$$

where, ϕ_1 is the angle between the flowline in layer 1 and the interface of contact with layer 2, ϕ_2 is the angle between the deflected flowline in layer 2 and the interface of contact with layer 1. p_1 is the porosity of layer 1, and p_2 is the porosity of layer 2.

Figure 1 follows from the work of [29], which highlighted the deflection phenomenon of fluid flow line at the interface of contact of two different media characterized by different average permeabilities and its applicability to the seepage process of dams. Forchheimer was suggested to have probably been the first to observe this property in the early 1900s, but never took the trouble of making a publication on it. [30] discussed the deflection at the interface of different media as a refraction-like phenomenon, forcing the travelling fluid to spend the greatest distance possible in the path/section of least resistance, which is the most permeable medium. This has been reverified by many recent experimental works, which have also exposed the flow characteristics resulting from the refraction like phenomenon and corresponding application in the control of contaminated fluids [3], [4], [24], [27], [31], [32]. A few of the works are discussed briefly below.

From laboratory experiment, a generalized relationship between the angle of deflection of a fluid flowing through two interfaces and porosity ratio of the interface was established as:

$$\theta = 22.85 + 310.08\varphi_r - 352.77\varphi^2 \quad (5)$$

where θ is the angle of deflection in degrees, and φ_r is the porosity ratio between the interface [31]. The relationship of the cosine of the angle of deflection to porosity ratio was obtained as:

$$cos\theta = 1.98ln\varphi_r + 1.13 \quad (6)$$

where θ is the angle of deflection in degrees, and φ_r is the porosity ratio between the interface [32].

[33], through laboratory experiment explored the velocity distribution curve parabola pattern based on Hagen-Poiseuille law. It was established that, for a circular pipe filled with layers of sand of different porosities, the velocity of a fluid passing through the pipe from the lower to the higher permeable layer, increases from the centre to be maximum at the pipe wall. However, the velocity of the fluid increases from the wall to be maximum at the centre of the pipe, when flowing from the higher to lower permeable layer. Hence, the former arrangement could be suitable for deflecting contaminated fluids to the direction of choice. The work agrees with [3].

To the best of our knowledge, none of the previous works provided a model for fluid flow in both directions (a forward and reverse directional flow), based on volume flux as a function of angle of deflection. The two models available from the literature merged both types of flow and expressed a relationship between the angle of deflection and porosity ratio [31-32]. Also, such models are only applicable to environmental control problems.

In this work, we intend to relate volume flux to the angle of deflection as a model applicable to hydrocarbon reservoirs. Furthermore, a novel numerical method for combining models will be proposed. The extension of the flow system to hydrocarbon reservoirs is based on flow units as introduced by Dale Winland of American Chemical and Oil Company's (AMOCO) Research Department, as reported by [34]. In the Hartzog Draw reservoir study in Wyoming, USA, a flow unit was defined as a subdivision of a reservoir that is characterized by lateral and vertical continuity and has similar permeability, porosity, and bedding characteristics [35].

The data were obtained from the work of [33]. The inference from the paper was briefly discussed earlier. More details on how the data were obtained are available in the paper. The setup of the laboratory experiment satisfies the classification as a series of two different flow units since, from the available data, each sample is characterized by different porosity, permeability, grain size, and hydraulic conductivity. This should result in different storage capacity, flow capacity, and reservoir process speed [36]–[46].

II. Methodology

A plot was made from the data in Table 2. Figures (2-4) shows the plot of Volume Flux against Outlet Angle and the accompanying 3rd order polynomial regression model for the forward fluid flow (ABΔP, ACΔP, and ADΔP), while Figures (5-7) shows the reverse case (BAΔP, CAΔP, and DAΔP). The models generated for each plot and the associated statistics summary are shown in Table 3.

To deduce a generalized model from the six models (3 for the forward, and 3 for the reverse directional flow), a solution has to be found that solves the three systems of the equation for each directional flow.

A. Pseudo-inverse matrix

Given three systems of equations which are the models generated from the plots for the forward directional flow of the form (same applies to the reverse case):

$$\begin{aligned} V_1 &= A_1x + B_1y + C_1z + D_1k \\ V_2 &= A_2x + B_2y + C_2z + D_2k \\ V_3 &= A_3x + B_3y + C_3z + D_3k \end{aligned} \tag{7}$$

These systems of equations can be re-written in matrix form [47], [48]:

$$\begin{pmatrix} V_1 \\ V_2 \\ V_3 \end{pmatrix} = \begin{pmatrix} A_1 & B_1 & C_1 & D_1 \\ A_2 & B_2 & C_2 & D_2 \\ A_3 & B_3 & C_3 & D_3 \end{pmatrix} \cdot \begin{pmatrix} x \\ y \\ z \\ k \end{pmatrix} \tag{8}$$

$$V = \begin{pmatrix} V_1 \\ V_2 \\ V_3 \end{pmatrix} \tag{9}$$

$$F = \begin{pmatrix} A_1 & B_1 & C_1 & D_1 \\ A_2 & B_2 & C_2 & D_2 \\ A_3 & B_3 & C_3 & D_3 \end{pmatrix} \tag{10}$$

$$M = \begin{pmatrix} x \\ y \\ z \\ k \end{pmatrix} \tag{11}$$

This results in:

$$V = F \cdot M \tag{12}$$

Making *M(x,y,z,k)* the subject of the formula:

$$\frac{V}{F} = M \tag{13}$$

Therefore;

$$F^{-1} \cdot V = M \tag{14}$$

Table 1: Values for Porosity, Hydraulic Conductivity, and Permeability for Sand Samples A-D [33]

Sample	Porosity	Hydraulic Conductivity (K) x 10^{-4} (ms^{-1})	Permeability (k) x 10^{-11} (m^2)
A	0.250 ± 0.010	0.460	0.470
B	0.333 ± 0.002	1.010	1.060
C	0.364 ± 0.001	1.140	1.160
D	0.420 ± 0.010	3.290	3.360

Table 2: Volume Flux at various Outlet Angles for Ascending Layer Heterogenous (ALH) and Descending Layer Heterogenous (DLH)) [33].

	Volume Flux for Ascending Order of Porosity (ALH)			Volume Flux for Descending Order of Porosity (DLH)		
Angle of Outlets (°)	ABΔP = 0.083 q x 10^{-4} (ms^{-1})	ACΔP = 0.114 q x 10^{-4} (ms^{-1})	ADΔP = 0.170 q x 10^{-4} (ms^{-1})	BAΔP = 0.083 q x 10^{-4} (ms^{-1})	CAΔP = 0.114 q x 10^{-4} (ms^{-1})	DAΔP = 0.170 q x 10^{-4} (ms^{-1})
0	0.0047	0.0071	0.0141	0.1543	0.1543	0.1760
20	0.0071	0.0071	0.0153	0.1095	0.1272	0.1398
50	0.0518	0.0542	0.0130	0.0448	0.0730	0.0836
70	0.0506	0.0495	0.0683	0.0247	0.0306	0.0836
90	0.0071	0.0141	0.0612	0	0	0

**Note:
ABΔP is the change in porosity between sample A and B
ACΔP is the change in porosity between sample A and C
ADΔP is the change in porosity between sample A and D
BAΔP is the change in porosity between sample A and B
CAΔP is the change in porosity between sample A and C
DAΔP is the change in porosity between sample A and D
A negative sign is absent for the reverse (DLH) case because porosity cannot be negative

The limitation now comes up, in the process of mathematically obtaining the inverse of the matrix denoted by *F*. This is because the matrix is non-square. Instead, it can be described as a rectangular matrix, meaning the prerequisite determinant needed to obtain an inverse cannot be computed [49]. This is a product of an under-determined system, with more unknowns than the number of equations [49]. Of course, this is not unusual for laboratory experiments, where the trial measurement are sometimes limited due to circumstances beyond the control of researchers.

Since it is impossible to find F^{-1}, the pseudo inverse (F^{+}) can be employed. This is also known as the Moore-Penrose Generalized Inverse (MPGI). It gives a vector *M* that

makes $V - FM = 0$ from equation (12), closest to zero [49]–[53]. From equation (7), since there are more unknowns compared to the number of equations, this results in the number of rows (m = 3) being lesser than the columns (n = 4) as seen in equation (10). Therefore, *F* is of a row ranked matrix type, which commands the use of the right pseudo-inverse (equation 15). Of course, this could be fully ranked or not, depending on the matrix obtained after row reduction [49, 53]:

$$F^{+} = F^{T} \cdot (F \cdot F^{T})^{-1} \quad (15)$$

Since the pseudo-inverse solutions that are obtainable are infinite, it is then important to be able to choose the unique solution, that guarantees a minimum Euclidean norm ([52]–[54]. Such a solution is also known as the MPGI, and satisfies the following properties [50, 51, 53]:

$$\begin{aligned} &F \cdot F^{+} \cdot F = F \\ &F^{+} \cdot F \cdot F^{+} = F^{+} \\ &(F \cdot F^{+})^{T} = F \cdot F^{+} \\ &(F^{+} \cdot F)^{T} = F^{+} \cdot F \end{aligned} \quad (16)$$

Equation (15) is not adequate in handling round-off errors and other numerical problems [49], [52], [55]. The Singular Value Decomposition (SVD) is a good alternative. It is efficient and can be run with the help of Maple software, 2020 edition. It works as a method for decomposition any matrix into three components, of which the pseudo-inverse can easily be found [52], [54], [55]:

$$F = UDV^{T} \quad (17)$$

Equation (18) gives the MPGI:

$$F^{+} = VD^{+}U^{T} \quad (18)$$

where, $\in \mathcal{R}^{3x4}$; $U \in \mathcal{R}^{3x3}$; $D \in \mathcal{R}^{3x4}$; $V \in \mathcal{R}^{4x4}$; and $V \in \mathcal{R}^{4x4}$. Also, $VV^{T} = I = V^{T}V;\ UU^{T} = I = U^{T}U$.

It should be noted that F is the original matrix, V and U are unitary matrices, and D is a diagonal matrix [49, 57]. More details on SVD can be explored in the cited literature.

From equation (14), a new equation result;

$$F^{+} \cdot V \simeq M \quad (19)$$

Equation (19) is the formula for obtaining the matrix's solution (*M*).

B. Application of SVD for Pseudo-inverse

Equation (20) and (21) shows the three obtained models for ALH and DLH plot of volume flux against outlet angle respectively (Fig. 2-4 and 5-7). The equations have been truncated to aid comprehension, but the full numerical values were used in the calculations.

$$\begin{aligned} V_{AB} &= -6.17 * 10^{-7}\theta^{3} + 6.47 * 10^{-5}\theta^{2} - \\ &\quad 8.05 * 10^{-4}\theta + 4.09 * 10^{-3} \\ V_{AC} &= -5.76 * 10^{-7}\theta^{3} + 6.13 * 10^{-5}\theta^{2} - \\ &\quad 7.78 * 10^{-4}\theta + 6.00 * 10^{-3} \\ V_{AD} &= -3.07 * 10^{-7}\theta^{3} + 4.98 * 10^{-5}\theta^{2} - \\ &\quad 1.47 * 10^{-3}\theta + 1.74 * 10^{-2} \end{aligned} \quad (20)$$

Where, $V_{AB}, V_{AC}, \text{and } V_{AD}$ are volume flux for flow from sand sample A to B, A to C, and A to D, respectively. θ is the outlet angle.

$$\begin{aligned} V_{BA} &= -6.60 * 10^{-9}\theta^{3} + 9.23 * 10^{-6}\theta^{2} - \\ &\quad 2.60 * 10^{-3}\theta + 1.55 * 10^{-1} \\ V_{CA} &= 1.48 * 10^{-7}\theta^{3} - 2.23 * 10^{-5}\theta^{2} - \\ &\quad 9.06 * 10^{-4}\theta + 1.54 * 10^{-1} \\ V_{DA} &= -5.23 * 10^{-7}\theta^{3} + 6.42 * 10^{-5}\theta^{2} - \\ &\quad 3.49 * 10^{-3}\theta + 1.79 * 10^{-1} \end{aligned} \quad (21)$$

Where, $V_{BA}, V_{CA}, \text{and } V_{DA}$ are volume flux for flow from sand sample B to A, C to A, and D to A, respectively.

Using the models in equations (20) and (21), a generalized model can be obtained for each of the sample's arrangements (ascending and descending). This follows the concept of the addition of vector spaces covered by each

model to obtain a generalized model for each system of arrangement [58]–[60]. We will be referring to this model as the Vector Space Model (VSM):

$$V_{ALH} = -1.50 * 10^{-6}\theta^3 + 1.76 * 10^{-4}\theta^2 - 3.05 * 10^{-3}\theta + 2.75 * 10^{-2} \quad (22)$$

$$V_{DLH} = -3.68 * 10^{-7}\theta^3 + 5.11 * 10^{-5}\theta^2 - 7.00 * 10^{-3}\theta + 4.88 * 10^{-1} \quad (23)$$

where,

$$V_{ALH} = V_{AB} + V_{AC} + V_{AD}\text{, and } V_{DLH} = V_{BA} + V_{CA} + V_{DA}$$

But, we intend to propose another New Model (NM). From equation (20) and (21), a matrix of the form of equation (8) can be obtained, with η, α, β, and γ equal to $\theta^3, \theta^2, \theta^1, \text{and } \theta^0$ respectively.

$$\begin{pmatrix} V_{AB} \\ V_{AC} \\ V_{AD} \end{pmatrix} = \begin{pmatrix} -6.60 * 10^{-9} & 6.47 * 10^{-5} & -8.05 * 10^{-4} & 4.09 * 10^{-3} \\ -5.76 * 10^{-7} & 6.13 * 10^{-5} & -7.78 * 10^{-4} & 6.00 * 10^{-3} \\ -3.07 * 10^{-7} & 4.98 * 10^{-5} & -1.47 * 10^{-3} & 1.74 * 10^{-2} \end{pmatrix} \cdot \begin{pmatrix} \eta \\ \alpha \\ \beta \\ \gamma \end{pmatrix} \quad (24)$$

$$\begin{pmatrix} V_{BA} \\ V_{CA} \\ V_{DA} \end{pmatrix} = \begin{pmatrix} -6.60 * 10^{-9} & 9.23 * 10^{-6} & -2.60 * 10^{-3} & 1.55 * 10^{-1} \\ 1.48 * 10^{-7} & -2.23 * 10^{-5} & -9.06 * 10^{-4} & 1.54 * 10^{-1} \\ -5.23 * 10^{-7} & 6.42 * 10^{-5} & -3.49 * 10^{-3} & 1.79 * 10^{-1} \end{pmatrix} \cdot \begin{pmatrix} \eta \\ \alpha \\ \beta \\ \gamma \end{pmatrix} \quad (25)$$

Making the outlet angle parameters the subject of the formula for equations (24) and (25) in line with equation (19) results in;

$$\begin{pmatrix} -6.60 * 10^{-9} & 6.47 * 10^{-5} & -8.05 * 10^{-4} & 4.09 * 10^{-3} \\ -5.76 * 10^{-7} & 6.13 * 10^{-5} & -7.78 * 10^{-4} & 6.00 * 10^{-3} \\ -3.07 * 10^{-7} & 4.98 * 10^{-5} & -1.47 * 10^{-3} & 1.74 * 10^{-2} \end{pmatrix}^{+} \cdot \begin{pmatrix} V_{AB} \\ V_{AC} \\ V_{AD} \end{pmatrix} = \begin{pmatrix} \eta \\ \alpha \\ \beta \\ \gamma \end{pmatrix} \quad (26)$$

$$\begin{pmatrix} -6.60 * 10^{-9} & 6.47 * 10^{-5} & -8.05 * 10^{-4} & 4.09 * 10^{-3} \\ -5.76 * 10^{-7} & 6.13 * 10^{-5} & -7.78 * 10^{-4} & 6.00 * 10^{-3} \\ -3.07 * 10^{-7} & 4.98 * 10^{-5} & -1.47 * 10^{-3} & 1.74 * 10^{-2} \end{pmatrix}^{+} \cdot \begin{pmatrix} V_{BA} \\ V_{CA} \\ V_{DA} \end{pmatrix} = \begin{pmatrix} \eta \\ \alpha \\ \beta \\ \gamma \end{pmatrix} \quad (27)$$

Running the SVD algorithm to obtain the pseudo inverse of the 3x4 matrices in equations (26) and (27) gives the 4x3 matrices of equations (28) and (29). Assuming a volume flux range of 0-0.2148 ms^{-1}, a set of solutions can then be estimated for the outlet angle parameters. The chosen volume flux range is not out of place with the experiment data, since from Table 2, there is a range of 0-0.1760 ms^{-1}. The assumed values are subsequently referred to as the Volume Flux for Model (VFM).

$$\begin{pmatrix} 515.65 & -883.40 & 183.91 \\ -44403.55 & 76119.86 & -15854.05 \\ -7299.58 & 8782.86 & -1317.62 \\ -489.77 & 524.19 & -8.36 \end{pmatrix} \cdot \begin{pmatrix} 0 \\ 0 \\ 0 \end{pmatrix} = \begin{pmatrix} \eta \\ \alpha \\ \beta \\ \gamma \end{pmatrix} \quad (28)$$

$$\begin{pmatrix} 362.48 & -74.61 & -249.92 \\ -32807.21 & 6747.59 & 22624.60 \\ -1212.52 & 725.77 & 426.45 \\ -11.89 & 11.74 & 5.79 \end{pmatrix} \cdot \begin{pmatrix} 0 \\ 0 \\ 0 \end{pmatrix} = \begin{pmatrix} \eta \\ \alpha \\ \beta \\ \gamma \end{pmatrix} \quad (29)$$

Note**: For equations (28) and (29), VFM = 0 was used as the starting point of the iteration, hence the 3x1 matrices on the left-hand side. The summary table of the obtained outlet angle parameters for each corresponding VFM for ALH and DLH is shown in Appendix Table 1.

A plot of the VFMs against corresponding outlet angle parameters was made for ALH and DLH, to reveal a relationship between volume flux and the deflection of flow (outlet angle). Figures (8-10) show the plots. The statistical tool known as Mean Absolute Error (MAE) was employed to choose the best model. Tables (3) and (4) show the statistics summary table for the ALH and DLH,

respectively. Equation (30) shows the employed formula;

$$MAE = \frac{\sum_{i=1}^{12} |Outlet\ Angel\ Parameter_i - VFM_i|}{12} \quad (30)$$

To conclude the research, Table (5) shows the average volume flux from the experiment, volume flux estimated from VSM, and volume flux estimated from NM. This was obtained by substituting the known angles into equations (22) and (23), and that of NM.

III. Result and Discussion

A. Ascending Layer Heterogeneous (ALH)

Figures (2-4) show the plot of experimental volume flux against outlet angle (solid blue line) and a 3rd order polynomial model fit (red dash line) for ALH. From Figures (2-4), it can be observed that the volume flux for all the sand samples experiences a peak at around 60°, except for sample AD, where there was a shift to about 65°. This is in line with the findings of [33]. A proposition can be made that, at lower angles of outlet angle (specifically 0°) for ALH, a lower volume flux can be expected, but this is not absolute within all porosity limits, as observed in sample AD (Figure 4), where a volume flux even lower than that experienced in 0° was later recorded at about 40° outlet angle [3], [22], [27], [31], [32]. Furthermore, although there is limited data, it can be inferred that, with an increase in the porosity difference between two media, the volume flux at the interface associated with right angles will tend to increase. This can be observed with the volume flux at 90° outlet angle in Figures (2-4).

In addition, the models show increased divergence as the porosity difference between interfaces increases. The plots for sample AB and AC (Figures 2 and 3) have R2 value of 0.99 and 0.97 respectively, while sample AD (Figure 4) have 0.80. This implies that, even for the lowest R2, value model, 80% of the

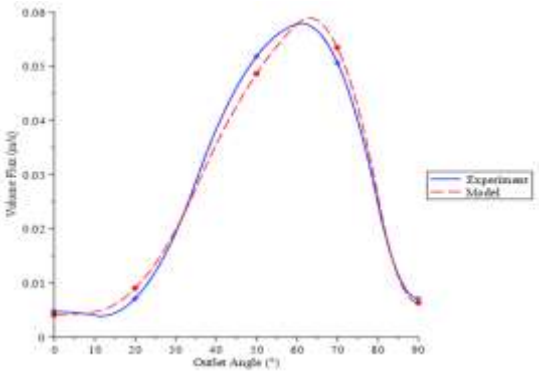

Figure 2: Plot of experimental volume flux against outlet angle for sample AB

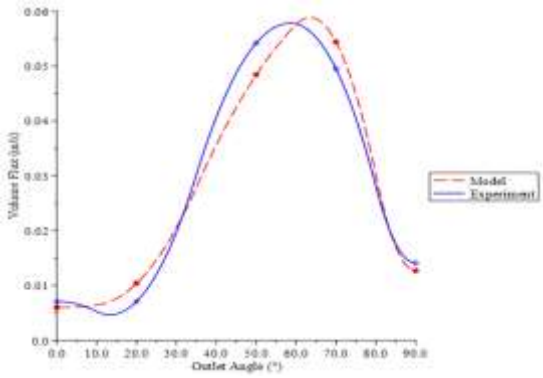

Figure 3: Plot of experimental volume flux against outlet angle for sample AC

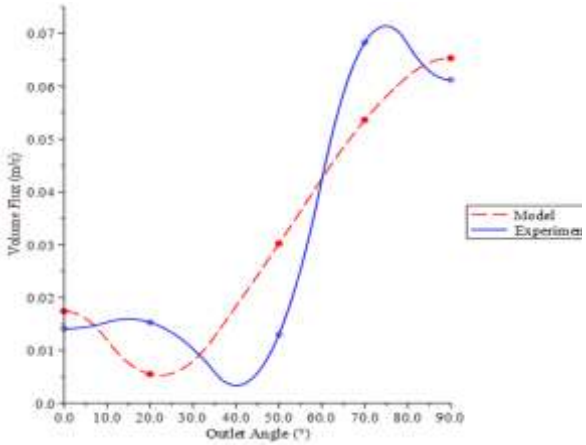

Figure 4: Plot of experimental volume flux against outlet angle for sample AD

dependent variable (volume flux) can be explained by the independent variable (outlet angle). Although small sample data can make R^2 biased, it remains the best statistical tool to judge the fitness of models [61-63]. Therefore, the 3rd order polynomial models as expressed by equation (20) for the ALH are all of a good fit.

i. Pseudo-inverse for ALH

Table 1a in the appendix shows the estimated outlet angle parameters, obtained from the numeration using SVD. The plot of the VFM against each of the parameters is shown in Figures (5-7). The plot in Figure (5) stands out because of the negative values of the outlet angle parameter ŋ. This is not out of place because the pseudo-inverse used in estimating the outlet angle parameters is a least square method. This means, obtaining values that seem out of place cannot be ruled out since only the unique matrix that satisfies the MPGI properties is acceptable [52], [53].

The three plots (Figures 5-7) have an R^2 value of 1.00 each, which shows that the independent variables account for all the independent variables. The equation of model for each parameter is:

$$V_{ŋ} = -5.44 * 10^{-3}ŋ + 6.74 * 10^{-17} \quad (31)$$

$$V_{\alpha} = 6.30 * 10^{-5}\alpha - 1.12 * 10^{-17} \quad (32)$$

$$V_{\beta} = 6.04 * 10^{-3}\beta - 1.04 * 10^{-16} \quad (33)$$

where, $V_{ŋ}, V_{\alpha}$ and V_{β} are the estimated volume flux using the $ŋ, \alpha$ and β parameters, respectively. $ŋ, \alpha$ and β are the estimated outlet angles or deflection angles.

ii. Back-testing Models for ALH

Mean Absolute Error (MAE), which is a statistical tool, was used to determine the most accurate model between NM (equation 33) and VSM (equation 22) for the ALH model. The actual experimental data (Table 2) was the source of input for both models, resulting in Table 4.

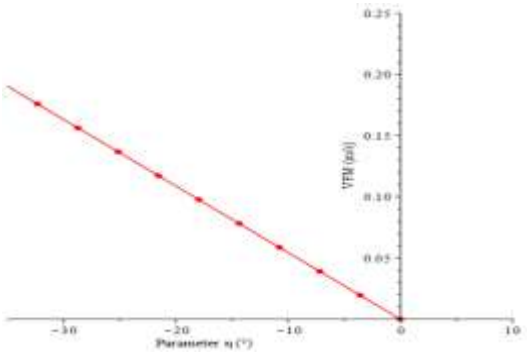

Figure 5: Plot of VFM against outlet angle parameter ŋ

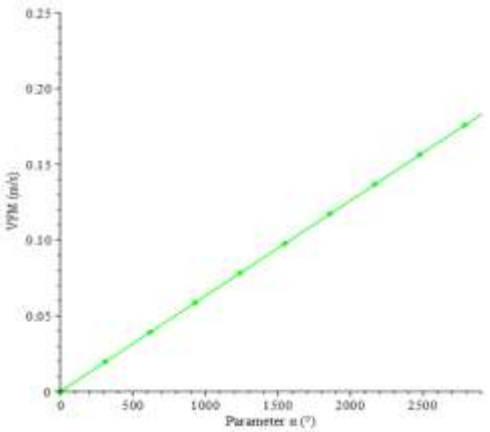

Figure 6: Plot of VFM against outlet angle parameter α

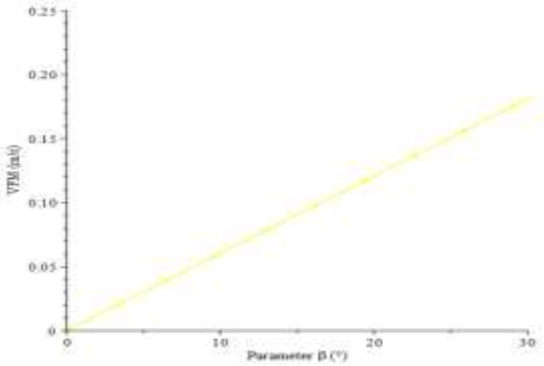

Figure 7: Plot of VFM against outlet angle parameter β

iii. Mean Absolute Error (MAE) for ALH

Table 3: Statistics summary table to estimate the model with the least Mean Absolute Error (MAE) for ALH

VFM	ŋ	|ŋ-VFM|	α	|α-VFM|	β	|β-VFM|
0	0	0	0	0	0	0
0.0195	0.0194	0.0001	0.01951	0	0.0194	0.0001
0.0390	0.0388	0.0003	0.0390	0	0.0388	0.0002
0.0586	0.0582	0.0004	0.0586	0	0.0582	0.0004
0.0781	0.0776	0.0006	0.0781	0.0001	0.0777	0.0005
0.0977	0.0969	0.0007	0.0976	0.0001	0.0971	0.0005
0.1172	0.1163	0.0009	0.1171	0.0001	0.1165	0.0007
0.1367	0.1357	0.0010	0.1366	0.0001	0.1359	0.0008
0.1562	0.1551	0.0011	0.1561	0.0002	0.1553	0.0009
0.1758	0.1745	0.0013	0.1757	0.0001	0.1747	0.0011
0.1953	0.1939	0.0014	0.1952	0.0001	0.1941	0.0012
0.2148	0.2133	0.0016	0.2147	0.0002	0.2135	0.0013

Using equation (31), the β parameter (equation 33) with the MAE of 0.0007 has the lowest value, and hence is the best model

Table 4: Statistics Summary Table to Estimate the Model with the Lowest Mean Absolute Error (MAE) for ALH

Volume Flux for Ascending Order of Porosity (ALH)					
Outlet Angle (°)	Average ΔP = 0.122 q x 10^{-4} (ms^{-1})	VSM q x 10^{-4} (ms^{-1})	NM q x 10^{-4} (ms^{-1})	|VSM − Average| (ms^{-1})	|NM − Average| (ms^{-1})
0	0.0086	0.4882	0	0.4796	0.0086
20	0.0098	0.3658	0.1207	0.3560	0.1109
50	0.0397	0.2202	0.3018	0.1805	0.2621
70	0.0561	0.1228	0.4226	0.0667	0.3665
90	0.0275	0.0045	0.5433	0.0230	0.5158

**Note: Average ΔP is the average of the ABΔP, ACΔP, and ADΔP, and their corresponding volume

From equation (30):

$$MAE = \frac{\sum_{i=1}^{12} |Model_i - Average_i|}{5} \quad (34)$$

$$MAE_{VSM} = \frac{|1.1058|}{5} = 0.2212 \quad (35)$$

$$MAE_{NM} = \frac{|1.24669|}{5} = 0.2493 \quad (36)$$

From Table 4, it can be observed that the |NM-Average| column values have a greater divergence when compared to that of the |VSM-Average|column, from the Average ΔP column. This is verified by the MAE estimate of the VSM being lower than that of NM from equations (35) and (36), respectively. This means VSM is preferable to NM, but they can be used interchangeably since the difference in MAE is negligible.

B. Descending Layer Heterogeneous (DLH)

Figures (8-10) below show the plot of the experimental volume flux against the outlet angle for the samples BA, CA, and DA respectively. This is for the DLH. The fitted models are the dash red lines, while the experimental plots are the solid blue lines.

As observed by [33], the volume flux generally increases to become maximum at the zero-outlet angle (0°) in all the plots (Figures 8-10). This implies that the fluid's velocity profile when moving from a higher to lower porosity medium can be expected to be maximum at zero degrees angle of deviation from normal [4]. Samples BA (Figure 8) and CA (Figure 9) generally follow the same pattern, but that of DA (Figure 10) is more chaotic. This chaos was also observed in sample AD (Figure 4) for ALH. We believe this is a result of the increase in the porosity difference between the interfaces (for this case a sudden decrease in porosity), which implies more energy being needed to sustain flow.

This results in a chaotic flow, which can be described as a more non-darcian flow. Furthermore, as the porosity difference between interfaces increases, the models (dash red lines) show increased divergence from the actual data plot (solid blue lines). The model fit for all the plots is of 3rd order polynomial type, with an R^2 value of 1.00, 1.00, and 0.97

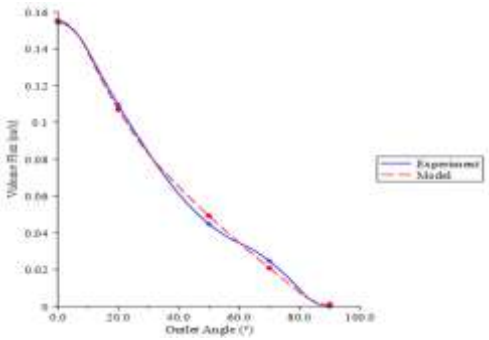

Figure 8: Plot of experimental volume flux against outlet angle for sample BA

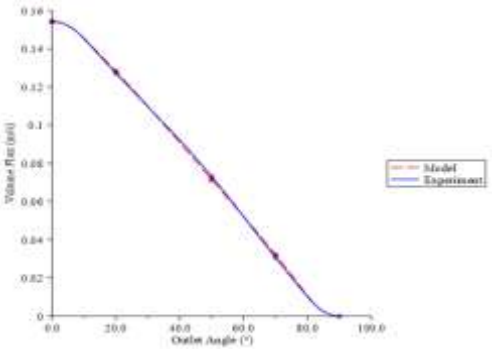

Figure 9: Plot of experimental volume flux against outlet angle for sample CA

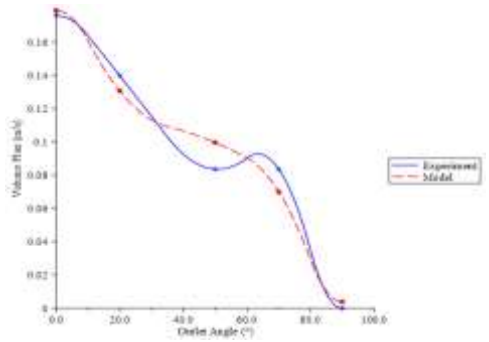

Figure 10: Plot of experimental volume flux against outlet angle for sample DA

respectively for samples BA, CA, and DA (Figure 8, 9, and 10).Taking into consideration the model with the lowest R^2 value (0.97), 97% of the dependent variable (volume flux) can be explained by the independent variable (outlet angle). Therefore, the 3rd order polynomial models as expressed by equation (21) for the DLH are all good fit.

i. Pseudo-inverse for DLH

Table 1a in the appendix shows the estimated outlet angle parameters, obtained from the numeration using SVD. The plot of the VFM against each of the parameters is shown in Figures (11-13). The plot in Figures (12 and 13) stands out because of the negative values of the outlet angle parameters α and β. This is not out of place as explained earlier. It is recommended that researchers try as much as possible to carry out many trial measurements during experimentation, to reduce the chances of dealing with an under-determined system. This will help to reduce errors and unexplainable values during numeration.

The three plots (Figures 11-13), have an R^2 value of 1.00 each, which shows that the independent variables account for all the dependent variables. The equation of model for each parameter is:

$$V_{\eta} = 2.64 * 10^{-2}\theta + 3.18 * 10^{-17} \quad (37)$$

$$V_{\alpha} = -2.91 * 10^{-4}\theta + 2.73 * 10^{-17} \quad (38)$$

$$V_{\beta} = -1.66 * 10^{-2}\theta - 1.50 * 10^{-17} \quad (39)$$

Where, V_{η}, V_{α} and V_{β} are the estimated volume flux using the η, α and β parameters, respectively. η, α and β are the estimated outlet angles or deflection angles.

ii. Mean Absolute Error (MAE) for DLH

Using equation (30), the β parameter equation (39) with the MAE of 0.0001 has the lowest value, but using the model is not feasible as it will yield negative volume flux values. Hence, the η parameter (Equation 37), which is the next best model in terms of low MAE value is suitable. This is not surprising, as only the plot of the η parameter (Figure 11) is on the positive side of the outlet angle parameter.

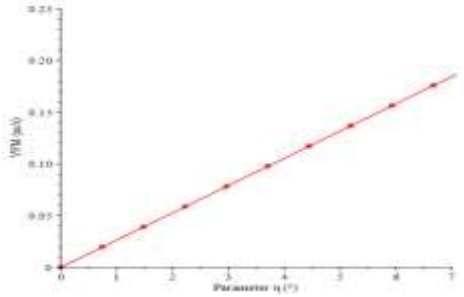

Figure 11: Plot of VFM against outlet angle parameter η

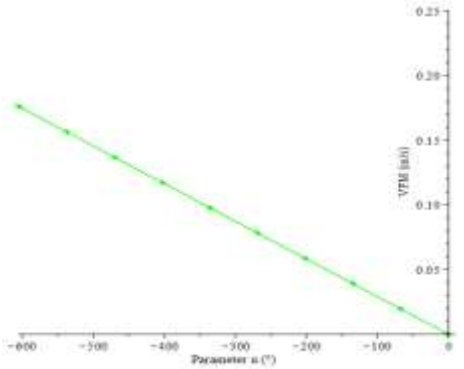

Figure 12: Plot of VFM against outlet angle parameter α

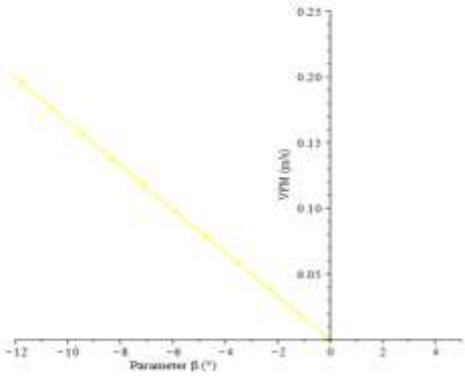

Figure 13: Plot of VFM against outlet angle parameter β

iii. Back-testing Models for DLH

To test the effectiveness of the NM (equation 35), in comparison to VSM (24) to model DLH, a back-testing has to be done with actual experiment data (Table 2). Table 6 shows the estimated volume flux values for the outlet angles (0, 20, 50, 70, and 90) substituted into the VSM and NM DLH

model equations, with the corresponding MAE statistical parameters.

$$MAE = \frac{\sum_{i=1}^{12}|Model_i - Average_i|}{5} \quad (40)$$

$$MAE_{VSM} = \frac{|0.801033|}{5} = 0.1602 \quad (41)$$

$$MAE_{NM} = \frac{|5.661033333|}{5} = 1.1322 \quad (42)$$

From Table 6, it can be observed that the |NM-Average| column values have a greater divergence when compared to that of the |VSM-Average|column, from the Average ΔP column. This is verified by the MAE estimate of the VSM being much lower than that of NM from equations (41) and (42), respectively. This means the VSM is more fit in modelling DLH than the NM.

C. Application to Reservoir Systems

As earlier stated, the experimental setup can be viewed as a local-scale combination of flow units, as a proxy for the system present in reservoirs. Therefore, a contributing factor to the less predictability of models in reservoirs can be attributed to the chaotic flow regime between flow units, as observed in our plots (Figures 4 and 10). But, the velocity profile should still follow our general observations:

i. The increase in the volume flux is to be maximum at a higher angle from normal when the fluid flows from flow units of lower to higher porosity (ALH).

ii. The decrease in volume flux from the maximum at the normal, to the minimum at the highest possible deviation from the normal, when flowing from a flow unit of higher to lower porosity (DLH). Of course, only an average porosity can be taken in the field from cores of different zones in a reservoir. Such properties gotten from cores are then used as the representative properties for the parent zones. This is also used in "extracting" the flow units that characterize reservoirs [16], [35], [39]–[41], [44]. Therefore, our propositions are not out of place. All that is needed is more sample taking to increase the cores' fitness to explain the parent properties accurately.

Table 5: Statistics Summary Table to Estimate the Model with the Mean Absolute Error (MAE) for DLH

VFM	ŋ	|ŋ-VFM|	α	|α-VFM|	β	|β-VFM|
0	0	0	0	0	0	0
0.0195	0.0196	0	0.0195	0.0001	0.0196	0
0.0390	0.0391	0.0001	0.0389	0.0002	0.0391	0
0.0586	0.0587	0.0001	0.0584	0.0002	0.0587	0.0001
0.0781	0.0783	0.0001	0.0778	0.0003	0.0782	0.0001
0.0977	0.0978	0.0002	0.0973	0.0004	0.0978	0.0001
0.1172	0.1174	0.0002	0.1167	0.0005	0.1173	0.0001
0.1367	0.1370	0.0002	0.1362	0.0005	0.1369	0.0001
0.1562	0.1565	0.0003	0.1556	0.0006	0.1564	0.0002
0.1758	0.1761	0.0003	0.1751	0.0007	0.1760	0.0002
0.1953	0.1956	0.0003	0.1946	0.0008	0.1955	0.0002
0.2148	0.2152	0.0004	0.2140	0.0008	0.2151	0.0002

Table 6: Statistics Summary Table to Estimate the Model with the Lowest Mean Absolute Error (MAE) for DLH

Volume Flux for Descending Order of Porosity (DLH)					
Outlet Angle (°)	Average ΔP = 0.122 q x 10^{-4} (ms^{-1})	VSM q x 10^{-4} (ms^{-1})	NM q x 10^{-4} (ms^{-1})	$\lvert VSM - Average \rvert$ (ms^{-1})	$\lvert NM - Average \rvert$ (ms^{-1})
0	0.1615	0.4882	0	0.3267	0.1615
20	0.1255	0.3658	0.5271	0.2403	0.4016
50	0.0671	0.2202	1.3177	0.1531	1.2506
70	0.0463	0.1228	1.8448	0.0765	1.7985
90	0	0.0045	2.3719	0.0045	2.3719

**Note: Average ΔP is the average of the BAΔP, CAΔP, and DAΔP, and their corresponding

The probable flow path can be predicted once the flow units are known for their porosity. Such prediction would help correlate with other data in being precise about the location of accumulation, leading to less expense in drilling exploratory wells.

IV. Conclusion

A laboratory experiment with heterogeneous layered media has been extended to the concept of flow units in hydrocarbon reservoir systems. The results showed that, when fluid flows from a flow unit of lower to that of higher porosity, a maximum volume flux is experienced at higher deflection angles from normal, and this tendency increases, with an increase in the porosity difference. On the other hand, a flow from a unit of higher to a lower porosity will result in the maximum volume flux being experienced at the normal, with decreasing magnitude as the deviation increases from normal. In addition, the flow becomes more chaotic and less predictable with the increase in porosity difference in both flow orders. But, it is crucial to note that, this flow system does not account for fractures.

For ALH, the VSM and NM could be used interchangeably because of the negligible difference in their MAE, while for the DLH, only the VSM can be used, due to a lower MAE value compared to NM. For ALH system of two flow units of average porosity difference 0.122 ms^{-1}, a VSM of: $V_{ALH} = -1.50 * 10^{-6}\theta^3 + 1.76 * 10^{-4}\theta^2 - 3.05 * 10^{-3}\theta + 2.75 * 10^{-2}$ was obtained, which could be used to estimate the volume flux from the known angle of deflection. In alternative, $V_\beta = 6.04 * 10^{-3}\beta - 1.04 * 10^{-16}$ can also be used, where β is the deflection angle, and V_β is the volume flux. For DLH flow units, the model $V_{DLH} = -3.68 * 10^{-7}\theta^3 + 5.11 * 10^{-5}\theta^2 - 7.00 * 10^{-3}\theta + 4.88 * 10^{-1}$ was obtained and this could be used to estimate volume flux V_{DLH} at a corresponding deflection angle (θ).

References

[1] Wang, H., Qian, H. and Gao, Y. "Non-darcian Flow in Loess at Low Hydraulic Gradient", *Engineering Geology*, vol. 267, 2020.

[2] Alabi, O.O. and Sedara, S.O. "Validity of Series and Parallel Bed Layer Permeability

Equations from Experimental and Numerical Modeling", *Scientific African*, vol. 10, 2020, pp. e00579.

[3] Popoola, O.I., Adegoke, J.A. and Alabi, O.O. "The Effects of Porosity and Angle of Inclination on the Deflection of Fluid Flow in Porous Media", *Global Journal of Pure and Applied Sciences*, vol. 15, no. 4, 2009, pp. 401–416.

[4] Alabi, O.O., Ojurongbe, T.A. and Sedara, S.O. "Gradients of Seepage Velocity Model for Contaminant Transport Prediction", *Scientific African*, vol. 4, 2019, pp. e00087.

[5] Sai, Y., Priya, J., Kumar, P.A. and Rao, B.R.S. "Modelling Recovery Process in Dual Porosity and Dual Permeability Reservoirs", *International Research Journal of Engineering and Technology*, 2020.

[6] Tiab, D. and Donaldson, E.C. "Porosity and Permeability", *Petrophysics*, Fourth Edition, Gulf Professional Publishing, 2016, pp. 67–186.

[7] Atapour, H. and Mortazavi, A. "The Effect of Grain Size and Cement Content on Index Properties of Weakly Solidified Artificial Sandstones", *Journal of Geophysics and Engineering*, vol. 15, no. 2, 2018, pp. 613–619.

[8] Yan-Long, L., Tie-Hang, W. and Li-Jun, S. "Determination of Bound Water Content of Loess Soils by Isothermal Adsorption and Thermogravimetric Analysis", *Soil Science*, vol. 180, no. 3, 2015, pp. 90–96.

[9] Li, S., Wang, C., Zhang, X., Zou, L. and Dai, Z. "Classification and Characterization of Bound Water in Marine Mucky Silty Clay", *Journal of Soils and Sediments*, vol. 19, no. 5, 2019, pp. 2509–2519.

[10] Noiriel, C., Steefel, C., Yang, L. and Bernard, D. "Effects of Pore-scale Precipitation on Permeability and Flow", *Advances in Water Resources*, vol. 95, 2016, pp. 125–137.

[11] Wetzel, M., Kempka, T. and Kühn, M. "Hydraulic and Mechanical Impacts of Pore Space Alterations within a Sandstone Quantified by a Flow Velocity-dependent Precipitation Approach", *Materials*, vol. 13, no. 14, 2020.

[12] Schepers, A. and Milsch, H. "Dissolution-precipitation Reactions in Hydrothermal Experiments with Quartz-feldspar Aggregates", *Contributions to Mineralogy and Petrology*, vol. 165, no. 1, 2013, pp. 83–101.

[13] Cil, M.B., Xie, M., Packman, A.I. and Buscarnera, G. "Solute Mixing Regulates Heterogeneity of Mineral Precipitation in Porous Media", *Geophysical Research Letters*, vol. 44, no. 13, 2017, pp. 6658–6666.

[14] Beckingham, L.E. "Evaluation of Macroscopic Porosity-Permeability Relationships in Heterogeneous Mineral Dissolution and Precipitation Scenarios", *Water Resources Research*, vol. 53, no. 12, 2017, pp. 10217–10230.

[15] Fazeli, H., Masoudi, M., Patel, R.A., Aagaard, P. and Hellevang, H. "Pore-Scale Modeling of Nucleation and Growth in Porous Media", *ACS Earth and Space Chemistry*, vol. 4, no. 2, 2020, pp. 249–260.

[16] Selley, R.C. and Sonnenberg, S.A. "The Reservoir", in *Elements of Petroleum Geology*, Third Edition., Boston: Academic Press, 2015, pp. 255–320.

[17] Murray, R.C. "Origin of Porosity in Carbonate Rocks", *SEPM Journal of Sedimentary Research*, vol. 30, 1960.

[18] Ma, S. and Morrow, N.R. "Relationships between Porosity and Permeability for Porous Rocks", *International symposium of the Society of Core Analysts*, January 1, 1996.

[19] Giatman, M., Haq, S. and Andayono, T. "Effect of Porosity on Soil Permeability in the Flood Area of Padang City", *Journal of Physics: Conference Series*, vol. 1387, no. 1, November 1, 2019, p. 012105.

[20] Hu, C., Agostini, F. and Jia, Y. "Porosity and Permeability Evolution with Deviatoric Stress of Reservoir Sandstone: Insights from Triaxial Compression Tests and in Situ Compression CT", *Geofluids*, vol. 2020, pp. 1–16.

[21] Bohnsack, D., Potten, M., Pfrang, D., Wolpert, P. and Zosseder, K. "Porosity–Permeability Relationship Derived from Upper Jurassic Carbonate Rock Cores to Assess the Regional Hydraulic Matrix Properties of the Malm

Reservoir in the South German Molasse Basin", *Geothermal Energy*, vol. 8, no. 1, 2020, pp. 12.

[22] Popoola, O.I., Adegoke, J.A. and Alabi, O.O. "A Laboratory Study of the Effects of Porosity on the Deviation from Darcy`s Law in Saturated Porous Media", *Research Journal of Applied Sciences*, vol. 2, no. 8, 2007, pp. 892–899.

[23] Popoola, O.I., Adegoke, J.A. and Alabi, O.O. "Modification of Darcy's Law for Turbulent Flow in Saturated Porous Media", *Research Journal of Applied Sciences*, vol. 2, no. 5, 2007, pp. 642–645.

[24] Alabi, O.O. "Fluid Flow in Homogeneous and Heterogeneous Porous Media", *Electronic Journal of Geotechnical Engineering*, vol. 16, no. A, 2011, pp. 61–70,

[25] Wen, X.H. and Gómez-Hernández, J.J. "Upscaling Hydraulic Conductivities in Heterogeneous Media: An Overview", *Journal of Hydrology*, vol. 183, no. 1–2, 1996, pp. ix–xxxii.

[26] Rajeh, T., Ababou, R., Marcoux, M. and Cañamon, I. "Fast Upscaling of the Hydraulic Conductivity of Three-Dimensional Fractured Porous Rock for Reservoir Modeling", *Mathematical Geosciences*, vol. 51, no. 8, 2019, pp. 1037–1074.

[27] Alabi, O.O. and Olaleye, K.O. "Modifying Hagen-Poiseullie's Equation for an Inclined Porous Media with Varying Porosity", *Journal of Indian Geophysical Union*, vol. 20, no. 20, 2016, pp. 231–240.

[28] Molins, S., Trebotich, D., Steefel, C.I. and Shen, C. "An Investigation of the Effect of Pore Scale Flow on Average Geochemical Reaction Rates using Direct Numerical Simulation", *Water Resources Research*, vol. 48, no. 3, 2012.

[29] Arthuh, C. "Seepage through Dams", *New England Water Works Association*, vol. LI, no. 2, 1937, pp. 131–172.

[30] Cedergren, R.H. "Seepage, Drainage, and Flow Nets", *3rd Edition*, vol. 16, New York: John Wiley & Sons, 1997.

[31] Popoola, O.I., Adegoke, J.A. and Alabi, O.O. "The Relationship between the Angle of Deflection and Porosity Ratio of Stratified Homogenous Porous Media", *Journal of Applied and Environmental Sciences*, vol. 6, no. 2, 2010, pp. 35–41.

[32] Popoola, O.I., Adegoke, J.A., Alabi, O.O., Akinluyi, F.O. and Fayemiwo, K.A. "Controlling Contaminated Fluid from Polluting Groundwater using Porous Media", *Journal of American Science*, vol. 6, no. 9, 2010.

[33] Alabi, O.O. "Velocity Profile of Fluid Flow in Heterogeneous Porous Media", *Electronic Journal of Geotechnical Engineering*, vol. 20, no. 3, 2015, pp. 943–952.

[34] Kolodzie, S. "Analysis of Pore Throat Size and Use of the Waxman-Smits Equation to Determine Ooip in Spindle Field, Colorado", SPE Annual Technical Conference and Exhibition, September 21, 1980.

[35] Hearn, C.L., Ebanks, W.J., Tye, R.S. and Ranganathan, V. "Geological Factors Influencing Reservoir Performance of the Hartzog Draw Field, Wyoming", *Journal of Petroleum Technology*, vol. 36, no. 08, 1984, pp. 1335–1344.

[36] Bear, J. "Dynamics of Fluids in Porous Media", New York: *Elsevier*, 1972.

[37] Ebanks, J.W.J. "Flow Unit Concept - Integrated Approach to Reservoir Description for Engineering Projects", *American Association of Petroleum Geologists Bulletin*, vol. 71, no. 5, 1987, pp. 551–552.

[38] Amaefule, J.O., Altunbay, M., Tiab, D., Kersey, D.G. and Keelan, D.K. "Enhanced Reservoir Description: Using Core and Log Data to Identify Hydraulic (Flow) Units and Predict Permeability in Uncored Intervals/Wells", SPE, 1993.

[39] Gunter, G.W., Finneran, J.M., Hartmann, D.J. and Miller, J.D. "Early Determination of Reservoir Flow Units Using an Integrated Petrophysical Method", SPE, 1997.

[40] Shedid, S.A. and Almehaideb, R.A. "Enhanced Reservoir Description of Heterogeneous Carbonate Reservoirs", *Journal of Canadian Petroleum Technology*, vol. 42, no. 07, 2003.

[41] Aguilera, R. "Flow Units: From Conventional to Tight-Gas to Shale-Gas to Tight-Oil to Shale-Oil Reservoirs", *SPE Reservoir*

Evaluation & Engineering, vol. 17, no. 02, 2014, pp. 190–208.

[42] Mahjour, S.K., Al-Askari, M.K.G. and Masihi, M. "Identification of Flow Units using Methods of Testerman Statistical Zonation, Flow Zone Index, and Cluster Analysis in Tabnaak Gas Field", *Journal of Petroleum Exploration and Production Technology*, vol. 6, no. 4, 2016, pp. 577–592.

[43] Mahjour, S.K., Al-Askari, M.K.G. and Masihi, M. "Identification of Flow Units using Methods of Testerman Statistical Zonation, Flow Zone Index, and Cluster Analysis in Tabnaak Gas Field", *Journal of Petroleum Exploration and Production Technology*, vol. 6, no. 4, 2016, pp. 577–592.

[44] Opuwari, M., Mohammed, S. and Ile, C. "Determination of Reservoir Flow Units from Core Data: A Case Study of the Lower Cretaceous Sandstone Reservoirs, Western Bredasdorp Basin Offshore in South Africa", *Natural Resources Research*, vol. 30, no. 1, 2021, pp. 411–430.

[45] Radwan, A.E., Nabawy, B.S., Kassem, A.A. and Hussein, W.S. "Implementation of Rock Typing on Waterflooding Process During Secondary Recovery in Oil Reservoirs: A Case Study, El Morgan Oil Field, Gulf of Suez, Egypt", *Natural Resources Research*, vol. 30, no. 2, 2021, pp. 1667–1696.

[46] Yi, D., Xiaobo, G. and Shuyun, C. "Research on Identification of Flow Units Based on FZI," *E3S Web of Conferences*, vol. 248, 2021, pp. 01005.

[47] Ross, C.T.F. "Matrix Algebra", *Advanced Applied Finite Element Methods*, Woodhead Publishing, 1998, pp. 21–67.

[48] Adu-Sackey, A., Lartey, G.O., Oduro, F.T. and Eduafo, S. "Cell Arrangement Method for Solving Systems of Linear Equations in Three Unknown", *Journal of Advances in Mathematics and Computer Science*, 2019, pp. 1–8.

[49] Kanan, M.A., Elbeleze, A.A. and Abubaker, A. "Applications of the Moore-Penrose Generalized Inverse to Linear Systems of Algebraic Equations", *American Journal of Applied Mathematics*, vol. 7, no. 6, 2019, pp. 152.

[50] Penrose, R. "A Generalized Inverse for Matrices", *Mathematical Proceedings of the Cambridge Philosophical Society*, vol. 51, no. 3, July 1955, pp. 406–413.

[51] Penrose, R. and Todd, J.A. "On Best Approximate Solutions of Linear Matrix Equations", *Mathematical Proceedings of the Cambridge Philosophical Society*, vol. 52, no. 1, 1956, pp. 17–19.

[52] Moloudzadeh, S., Darabi, P. and Khandani, H. "The Pseudo Inverse Matrices to Solve General Fully Fuzzy Linear Systems", *Journal of Soft Computing and Applications*, vol. 2013, pp. 1–11.

[53] Tan, L. "Generalized Inverse of Matrix and Solution of Linear System Equation", *A Generalized Framework of Linear Multivariable Control*, Butterworth-Heinemann, 2017, pp. 38–50.

[54] Golub, G.H. "Least Squares, Singular Values and Matrix Approximations", *Applications of Mathematics*, vol. 13, no. 1, 1968, pp. 44–51.

[55] Jason, L.S. and Walter, H.C. "4. Least Squares, the Orthogonal Projection Lemma, and Discrete-Time Kalman Filtering", *Stochastic Processes, Estimation, and Control*, Philadelphia: Society for Industrial and Applied Mathematics, 2008, pp. 119–151.

[56] Golub, G.H. and Reinsch, C. "Singular Value Decomposition and Least Squares Solutions", *Linear Algebra*, Berlin, Heidelberg: Springer Berlin Heidelberg, 1971, pp. 134–151.

[57] Hearon, J.Z. "Generalized Inverses and Solutions of Linear Systems", *Journal of Research of the National Bureau of Standards, Section B: Mathematical Sciences*, vol. 72B, no. 4, 1968, pp. 303.

[58] Curtis, M. and Tularam, A. "The Sum Two Reflective Polynomials and Its Link with the Proof of the Riemann Hypothesis", *Journal of Mathematics and Statistics*, vol. 10, no. 1, 2014, pp. 73–79.

[59] McAllister, L.M.N. "Finding a Base for a Vector Space of Polynomials", *Annual Meeting of the North American Fuzzy Information Processing Society - NAFIPS (Cat. No.97TH8297)*, 1997, pp. 283–285.

[60] Hearon, J.Z. "Minimum Polynomials and Control in Linear Systems", *Journal of Research of the*

National Bureau of Standards, vol. 82, no. 2, 1977, pp. 129

[61] Akossou, A., Akossou, A.Y.J. and Palm, R. "Impact of Data Structure on the Estimators R-Square and Adjusted R-Square in Linear Regression", *International Journal of Mathematics and Computation*, vol. 20, 2013, pp. 84–93.

[62] Valbuena, R., Hernando, A., Manzanera, J.A., Görgens, E.B., Almeida, D.R.A., Silva, C.A. and García-Abril, A. "Evaluating Observed Versus Predicted Forest Biomass: R-squared, Index of Agreement or Maximal Information Coefficient", *European Journal of Remote Sensing*, vol. 52, no. 1, 2019, pp. 345–358.

[63] Chicco, D., Warrens, M.J. and Jurman, G. "The Coefficient of Determination R-squared is more Informative than SMAPE, MAE, MAPE, MSE and RMSE in Regression Analysis Evaluation", *PeerJ Computer Science*, vol. 7, 2021, pp. e623.